

Article

Design of Polarization Splitter via Liquid and Ti Infiltrated Photonic Crystal Fiber

Qiang Xu ^{1,2,*}, Wanli Luo ^{1,†}, Kang Li ^{2,*} , Nigel Copner ² and Shebao Lin ¹

¹ College of Physics and Optoelectronic Technology, Baoji University of Arts and Sciences, Baoji 721016, China; 17789276164@163.com (W.L.); linshebao@163.com (S.L.)

² School of Engineering, University of South Wales, Cardiff CF37 1DL, UK; nigel.copner@southwales.ac.uk

* Correspondence: xuqiang@snnu.edu.cn (Q.X.); kang.li@southwales.ac.uk (K.L.); Tel.: +86-917-3364258 (Q.X.); +44-1443-482817 (K.L.)

† These authors contributed equally to this work.

Received: 31 January 2019; Accepted: 15 February 2019; Published: 18 February 2019



Abstract: We propose a new polarization splitter (PS) based on Ti and liquid infiltrated photonic crystal fiber (PCF) with high birefringence. Impacts of parameters such as shape and size of the air holes in the cladding and filling material are investigated by using a vector beam propagation method. The results indicate that the PS offers an ultra-short length of 83.9 μm , a high extinction ratio of -44.05 dB, and a coupling loss of 0.0068 dB and at 1.55 μm . Moreover, an extinction ratio higher than -10 dB is achieved a bandwidth of 32.1 nm.

Keywords: extinction ratio; polarization splitter; dual-core photonic crystal fiber; coupling characteristics

1. Introduction

Photonic crystal fiber (PCF) consists of a solid core and holes arranged in the cladding region non-periodically or periodically along the axis [1]. According to the mechanism of light transmission, PCF can be divided into refractive index guided PCF and photonic bandgap PCF. The refractive index guided PCF is similar to total internal reflection in the mechanism of light transmission. At present, refractive index guided PCF is the most mature and widely used optical fiber. PCF technology has made great progress in pharmaceutical drug testing, astronomy, communication, and biomedical engineering and sensing [2–8]. In recent years, the PCFs filled with materials have attracted great interests, because PCFs could provide excellent properties by filling different functional materials into the air holes [9–14]. Metal wire was filled into the air holes of PCFs for polarization splitting (PS) by Sun et al. and Fan et al. [10,11]. PCFs present high-quality channels that can be controllably filled with ultra-small volumes of analytes (femtoliter to subnanoliter), such as water [12], alcohol [13], and nematic liquid crystal [14].

The dual-core PCF is constructed by introducing two defect states in the periodic arrangement of air holes. When a polarized light beam is projected into the dual-core PCF with high birefringence, the coupling strength of two vertical polarization modes is weakened by the high birefringence [15]. Therefore, high birefringence could increase the difference in coupling length of the x -polarized mode and y -polarized mode of PCF, which is also beneficial to the miniaturization of PS. In general, high-birefringence fiber can be gained by breaking the symmetry implementing asymmetric defect structures, such as dissimilar air holes and elliptical holes along the two orthogonal axes, and asymmetric core design [16–18]. Another kind of high-birefringence fiber can also be manipulated by filling liquid into the air holes or hollow core [19]. At present, the dual-core PCF has a very mature application in polarization beam splitters.

The polarization handling devices based on PCFs filled with material, such as polarization splitters (PS) [20–22] and polarization rotators (PR) [23,24], have important applications in optical fiber sensing [25,26]. The PS could be divided into two fundamental modes (HE_{11}^x and HE_{11}^y) and propagate them in different directions. Its characteristics allow for significant applications in optical sensing, storage systems, communication systems, and integrated circuit systems [23,27]. In recent years, various PS structures based on PCFs have been reported in the literature [28–35]. These PS structures show good performance (see Table 1), such as an ultra-short length [31–33], a high extinction ratio [32], a low coupling loss [30,34], and an ultra-broad bandwidth [20,24,34], but these PS structures do not present these excellent properties at the same time. It is critical to design high-performance PS with ultra-short length, high extinction ratio, and low coupling loss [23]. In order to obtain a high-performance PS, we decided to use PCF filled with functional materials. It is well known that Ti demonstrates outstanding physical and chemical properties, such as light weight, anti-corrosion, biocompatibility, high melting point, durability, and high strength in extreme environments [36–38].

Table 1. Comparison of our proposed PS with earlier works.

References	Length/mm	Bandwidth/dB	Coupling loss/dB
[28]	1.7	40(<−11 dB)	not mentioned
[29]	4.72	190(<−20 dB)	not mentioned
[30]	8.7983	20(<−20 dB)	0.02
[31]	0.249	17(<−20 dB)	not mentioned
[32]	0.401	140(<−20 dB)	not mentioned
[33]	0.1191	249(<−20 dB)	not mentioned
[15]	14.662	13(<−10 dB)	not mentioned
[34]	4.036	430(<−20 dB)	0.011
[35]	0.775	32(<−20 dB)	not mentioned
Our work	0.0839	32.1(<−10 dB)	0.0068

In this paper, a novel ultra-short PS with low coupling loss and high birefringence is proposed based on the idea of material filled PCFs by using a vector beam propagation method (BMP) [39–41]. The numerical results present a 0.0839 mm-long PS with a coupling loss of 0.0068 dB and a high extinction ratio of −44.05 dB at the wavelength of 1.55 μm . Moreover, an extinction ratio higher than −10 dB is achieved at a bandwidth of 32.1 nm.

2. Physical Modeling

The physical modeling of the proposed PS is shown in Figure 1. The BPM-based commercially state-of-the-art software RSoft (Synopsys Inc., Mountain View, CA, USA) can be used to design and analyze optical telecommunication devices, optical systems and networks, optical components used in semiconductor manufacturing, and nano-scale optical structures. Figure 1 shows the structure of PS, where d , d_1 , d_2 , and d_3 represent the diameters of various air holes, respectively; a and b are the major and minor axes of the elliptical air hole; Λ represents distance of hole and hole (period); the ellipticity is expressed as $\eta = b/a$; and the air-filling ratio is d/Λ . The refractive index of background material is set as 1.45. Ti is filled into the two yellow air holes, and liquid (ethanol) is filled into the six blue holes. For ethanol ($\text{C}_2\text{H}_5\text{OH}$), variation of refractive index as a function of wavelength at a temperature of 20 °C is given by Reference [42].

$$n^2 - 1 = \frac{0.0165\lambda^2}{\lambda^2 - 9.08} + \frac{0.8268\lambda^2}{\lambda^2 - 0.01039} \quad (1)$$

where λ represents wavelength of the propagating light. The refractive index of ethanol is set as 1.35 at 1.55 μm . Figure 2 shows the refractive index function of Ti versus wavelength [43].

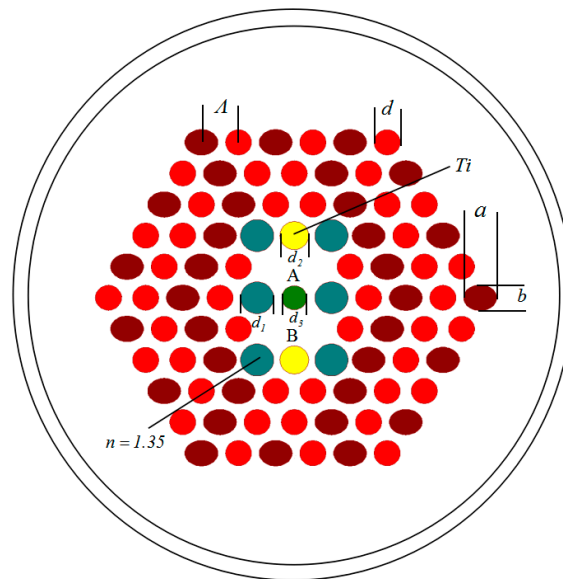


Figure 1. The cross-section of the proposed dual-core photonic crystal fiber (PCF).

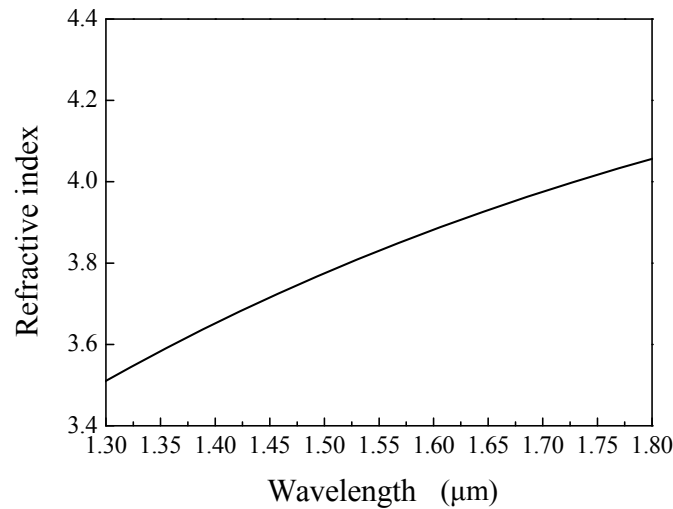


Figure 2. Refractive index of Ti as a function of wavelength [43].

The vector wave equation, which is the basis of BPM [39–41], can be expressed by

$$\nabla^2 \mathbf{E} + k^2 \mathbf{E} = 0 \tag{2}$$

$$\nabla^2 \mathbf{H} + k^2 \mathbf{H} = 0 \tag{3}$$

where $k \equiv \omega \sqrt{\mu \epsilon}$. These two equations are known as the Helmholtz equations.

The electric field $E(x, y, z)$ can be separated into two parts: the fast change term of $\exp(-ikn_0z)$ and the envelope term of $\phi(x, y, z)$ of slow change in the axial direction; n_0 is a refractive index in the cladding. Then, $E(x, y, z)$ is stated as

$$E(x, y, z) = \phi(x, y, z) \exp(ikn_0z) \tag{4}$$

Substituting Equation (4) in Equation (1) results in

$$\nabla^2 \phi - 2ikn_0 \frac{\partial \phi}{\partial z} + k^2(n^2 - n_0^2) = 0 \tag{5}$$

Assuming the weakly guiding condition, we can approximate $n^2 - n_0^2 \cong 2n_0(n - n_0)$. Then Equation (5) can be rewritten as

$$\frac{\partial \phi}{\partial z} = -i \frac{1}{2kn_0} \nabla^2 \phi + jk(n - n_0)\phi \quad (6)$$

A similar expression can be written for \mathbf{H} . We find that $n \neq n_0$ if the fields vary in the transverse direction to propagation. Light propagation in various kinds of waveguides can be analyzed by the above method.

There are four modes of dual-core PCF on the basis of the principle of coupling mode, namely, even-mode of x -polarization, odd-mode of x -polarization, even-mode of y -polarization, and odd-mode of y -polarization. The coupling length has been defined by Reference [44] as

$$L_c^{x,y} = \frac{\lambda}{2 |n_{even,\lambda}^{x,y} - n_{odd,\lambda}^{x,y}|} \quad (7)$$

where $n_{even}^{x,y}$, $n_{odd}^{x,y}$ denote the effective indexes of even-mode of x -polarization, odd-mode of x -polarization, even-mode of y -polarization, and odd-mode of y -polarization, respectively. When the coupling length of dual-core PCF satisfies $L = m L_c^x = n L_c^y$, the x -polarization and y -polarization launched into core A or B can be divided [33]. Hence, the coupling ratio (CR) can be defined as

$$CR = \frac{L_c^x}{L_c^y} = \frac{n}{m} \quad (8)$$

Assuming that the incident power is coupled into a certain core, the output power of x - or y -polarized light in the core can be expressed by the following equation [45]:

$$P_{out}^{x,y} = P_{in}^{x,y} \cos^2\left(\frac{\pi}{2} \cdot \frac{z}{L_c^{x,y}}\right) \quad (9)$$

where the transmission distance is denoted by z .

The extinction ratio is an important index to evaluate the performance of polarization splitter, which is expressed as

$$ER = 10 \log_{10} \left(\frac{P_{out}^x}{P_{out}^y} \right) \quad (10)$$

where P_{out}^x , P_{out}^y represent the output energy of x -polarization and y -polarization, respectively [16,46].

The coupling loss of the PS can be described by

$$Loss = -10 \log_{10} \left(\frac{P_{out}}{P_{in}} \right) \quad (11)$$

where P_{in} is the fundamental mode power at the input core [30].

Birefringence can be expressed as

$$B = |n_x - n_y| \quad (12)$$

where n_x and n_y are the effective refractive index of x -polarized and y -polarized fundamental modes [29].

3. Results and Discussion

First, the L_c and CR are examined for different period Λ , where $d_1 = 0.8 \mu\text{m}$, $d/\Lambda = 0.7$, $d_2 = 0.7 \mu\text{m}$, $\eta = 0.8$, and $d_3 = 0.6 \mu\text{m}$. The results are shown in Figure 3a, in which it is observed that the L_c is decreased when wavelength is increased for a constant period Λ . We also noticed that the L_c decreases with decreasing period Λ . Moreover, the coupling length of y -polarization is longer than the coupling length of x -polarization. As the period increases, the coupling between the cores becomes

difficult. Hence, the L_c increases with the increase of the period. Interestingly, from Figure 3b, we noticed that when $\Lambda \leq 1.1 \mu\text{m}$, the size of the CR is higher for higher period Λ ; when $\Lambda \geq 1.1 \mu\text{m}$, the size of the CR is higher for lower period Λ . According to Equation (8), when the CR is 3/4, the effective separation of the two orthogonal polarized lights can be achieved, so we choose the period value of $0.9 \mu\text{m}$.

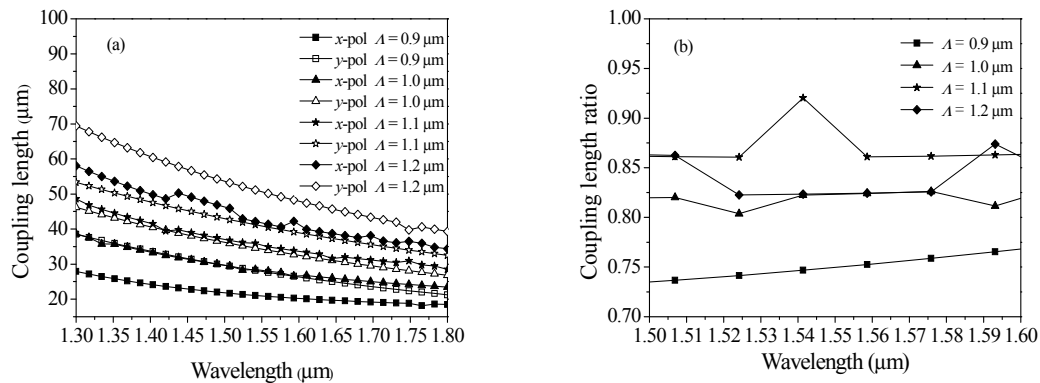


Figure 3. Coupling length (a) and coupling length ratio (b) as a function of wavelength for different period Λ .

Next, we analyze the L_c and CR as a function of wavelength for different air-filling ratio d/Λ , when $\eta = 0.8$, $d_2 = 0.7 \mu\text{m}$, $\Lambda = 0.9$, $d_3 = 0.6 \mu\text{m}$, and $d_1 = 0.8 \mu\text{m}$. From Figure 4a, it is observed that L_c is decreased when wavelength is decreased for the same value of air-filling ratio d/Λ . Moreover, we can find that the L_c decreases as the value of air-filling ratio increases, when air-filling ratio $d/\Lambda \leq 0.6$. This is owing to the restriction of the outer cladding to the light wave being enhanced as air-filling ratio increases. However, when $d/\Lambda \geq 0.6$, the result is opposite to the above. Meanwhile, the coupling length of y -polarization is longer than the coupling length of x -polarization. According to Figure 4b, it is found that when air-filling ratio $d/\Lambda \leq 0.6$, the size of the CR is higher for higher air-filling ratio d/Λ ; when air-filling ratio $d/\Lambda \geq 0.6$, the size of the CR is higher for lower air-filling ratio d/Λ . When we choose an air-filling ratio d/Λ of 0.7, the CR is approximately 3/4 at $1.55 \mu\text{m}$.

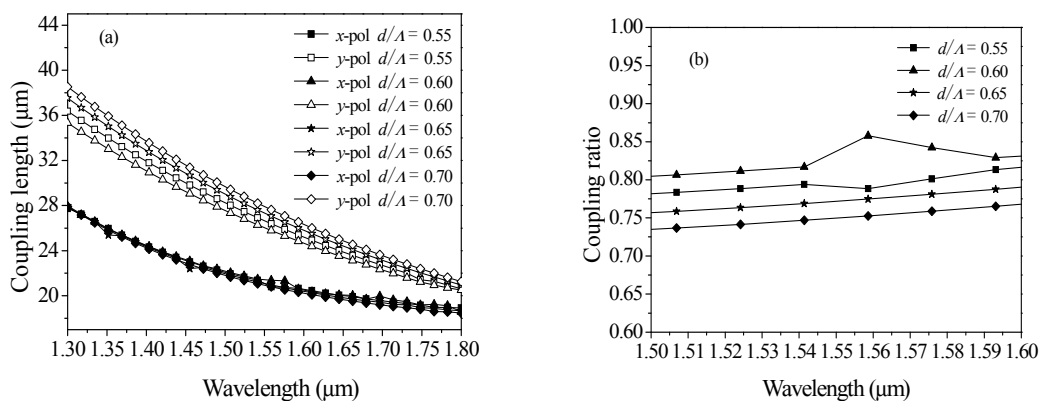


Figure 4. Coupling length (a) and coupling length ratio (b) as a function of wavelength for different air-filling ratio d/Λ .

Additionally, from Figure 5a, L_c is shown as a function of d_1 , in which it is observed that the coupling length is increased if d_1 is increased. This phenomenon can be interpreted as the following: as the value of d_1 increases, the cores of PS can be compressed in the vertical direction, and fundamental modes in the horizontal direction will expand. Figure 5a also indicates that x -polarized coupling length is lower than y -polarized coupling length. As seen in Figure 5b, the size of the CR increases with increasing wavelength. According to the above discussed results, we determine that d_1 is $0.8 \mu\text{m}$.

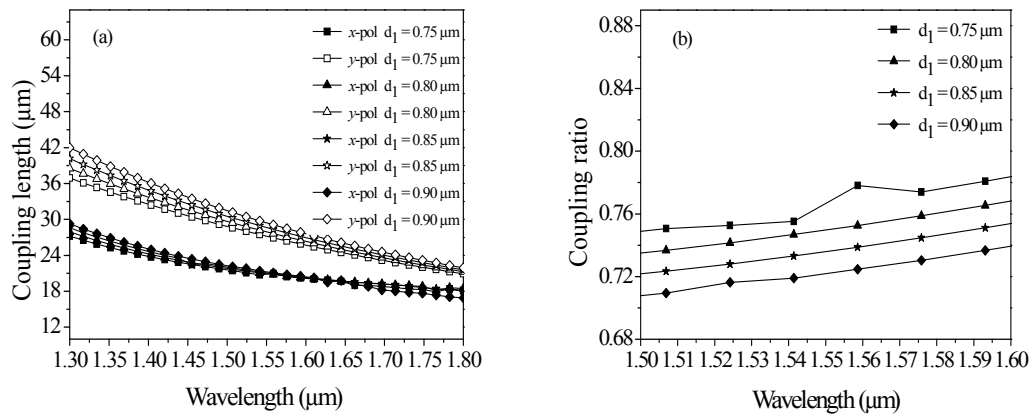


Figure 5. Coupling length (a) and coupling length ratio (b) as a function of wavelength for different d_1 .

Figure 6 shows d_2 dependence on the L_c (Figure 6a) and CR (Figure 6b). From Figure 6a, it is evident that the L_c^x decreases with increasing the value of d_2 . This result can be attributed to the following process: as the value of d_2 increases, the cores of PS can be compressed in the vertical direction, resulting in the increase of coupling length of y -direction. The L_c^y is shown as a function of d_2 in Figure 6a, in which it is observed that for $d_2 \leq 0.5 \mu\text{m}$, the value of CR is higher for higher d_2 ; for $d_2 \geq 0.5 \mu\text{m}$, the value of the CR is higher for lower d_2 . This phenomenon is probably related to the ratio of compression. According to Figure 6b, we can clearly see that the size of the CR increases with a decrease of d_2 . When the CR is $3/4$, the effective separation of the two orthogonal polarized lights can be achieved, so we choose the d_2 value of $0.7 \mu\text{m}$.

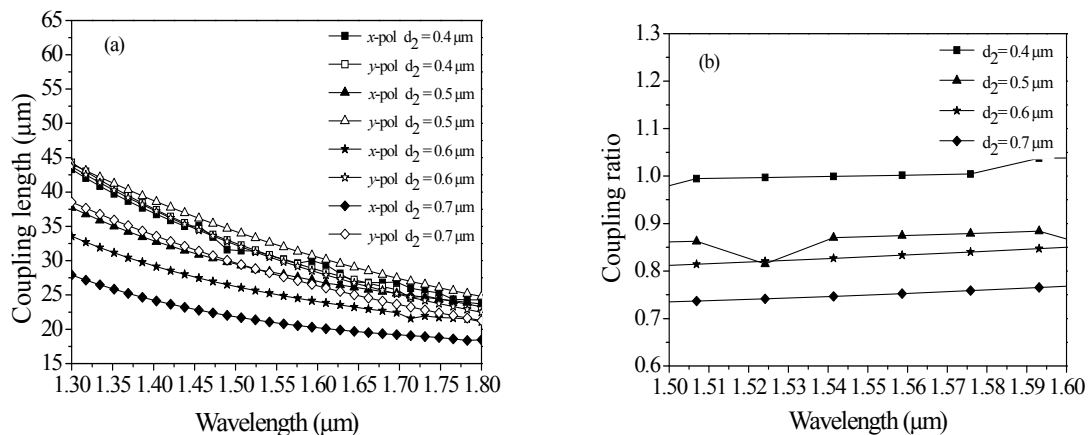


Figure 6. Coupling length (a) and coupling length ratio (b) as a function of wavelength for different d_2 .

The L_c and CR with the variation of wavelength are demonstrated in Figure 7, when $\eta = 0.65, 0.7, 0.75,$ and 0.8 . It can be found that the L_c reduces with respect to wavelength. Figure 7a indicates that L_c^y is higher than L_c^x . It can also clearly be seen that the four y -polarized curves are extremely close to each other. This result can be explained that as the ellipticity η increases, the cores of PS can be compressed vertically, and the fundamental mode in the horizontal direction will expand, which makes the coupling of two cores easier. According to Figure 7b, the size of the CR increases with decreasing ellipticity η . According to the above discussed results, we determine that η is 0.8 .

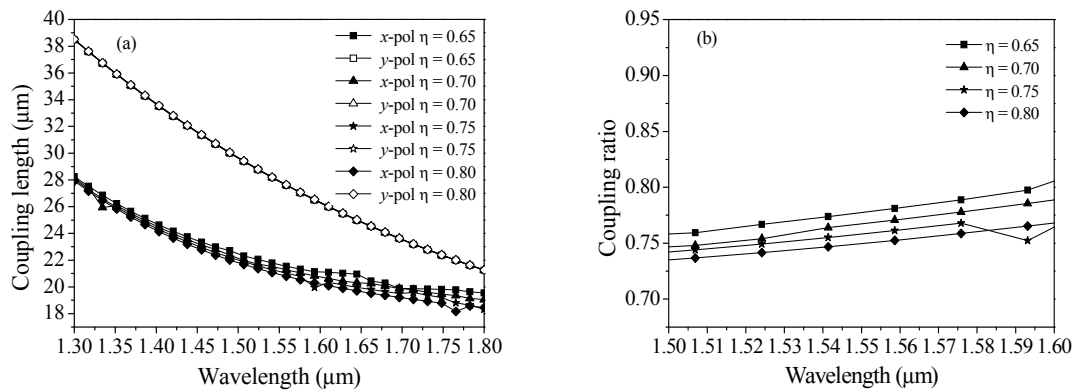


Figure 7. Coupling length (a) and coupling length ratio (b) as a function of wavelength for different η .

Finally, we found that the L_c and CR can both be impacted by d_1 , d_2 , d_3 , d/Λ , Λ , and η . Hence, there exist optimized structural parameters, namely, d_1 , d_2 , d_3 , Λ , d/Λ , and η is 0.8 μm , 0.7 μm , 0.6 μm , 0.9 μm , 0.7 and 0.8, respectively. Although the PS has many parameters, it can be easily influenced by the bulk polymerization process of polymers [47]. The optimized coupling length of x - and y -polarized direction are $L^x = 20.91 \mu\text{m}$ and $L^y = 27.96 \mu\text{m}$ at 1.55 μm , respectively. Figure 8 shows coupling characteristics of the PS. We observed that the separation of x - and y -polarized mode is achieved at the distance of 83.9 μm at 1.55 μm . Figure 9 shows the relationship between the birefringence and filling material for the optimized structural parameters. It is observed that birefringence of PS filled with liquid and Ti is higher than birefringence of PS filled with Ti. Meanwhile, the birefringence of PS filled with liquid and Ti can attain the order 10^{-2} at the wavelength of 1.55 μm , and the value of birefringence is about two orders of magnitude higher than that in References [29,48].

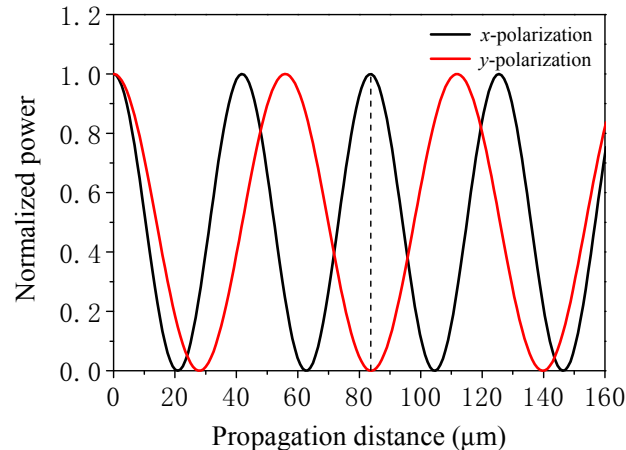


Figure 8. Normalized power as a function of propagation distance at optimized structural parameters.

Figure 10 shows the variation of coupling length with filling material for the optimized structural parameters. It can be seen that the coupling length of the PS with filled Ti is higher the coupling length of the PS with filled liquid and Ti. For the PS with filled Ti, coupling length of x - and y -polarized direction are $L^x = 29.25 \mu\text{m}$ and $L^y = 48.28 \mu\text{m}$ at 1.55 μm , respectively. According to Equation (8), the length of the PS with filled Ti is about 234 μm , which is much longer than the PS with filled liquid and Ti. Therefore, the PS filled with liquid and Ti has a shorter length and higher birefringence than the PS filled with Ti.

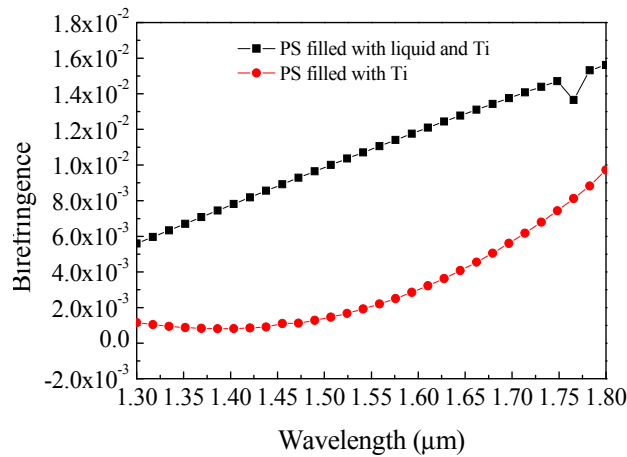


Figure 9. Birefringence as a function of wavelength for different filling materials.

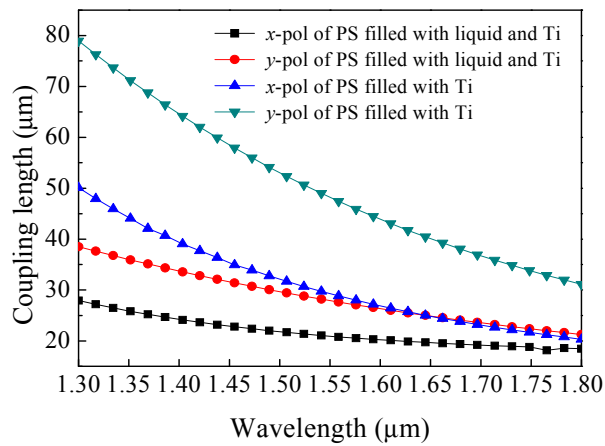


Figure 10. Coupling length as a function of wavelength for different filling materials.

Figure 11 shows the extinction ratio of PS with respect to wavelength at optimized structural parameters. The extinction ratio is measured in dB according to Equation (10). The PS has an extinction ratio of -44.05 dB at $1.55 \mu\text{m}$, an extinction ratio better than -10 dB, and a bandwidth of 32.1 nm from 1567 nm to 1535 nm. Figure 12 shows the coupling loss of PS as function of wavelength. We observe that the PS has a coupling loss of 0.0068 dB at $1.55 \mu\text{m}$. Performances in factors such as the length, coupling loss, and bandwidth are better than or at the same order of magnitude as those of the early works mentioned above (see Table 1).

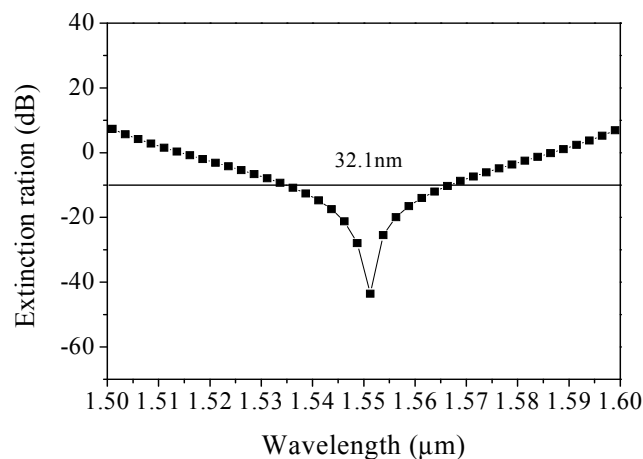


Figure 11. ER of PS as a function of wavelength at optimized structural parameters.

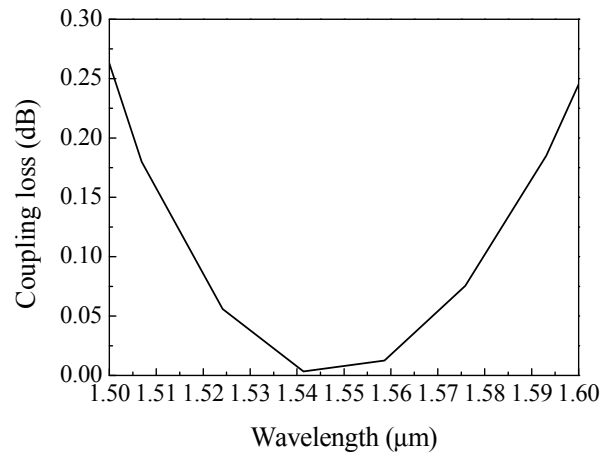


Figure 12. Coupling loss of PS as a function of wavelength at optimized structural parameters.

Figure 13 shows the mode field distribution of odd- and even-mode in x - and y -polarization direction. When a PS is incident upon core A or core B, both the odd- and even-mode of that polarization can be generated [49].

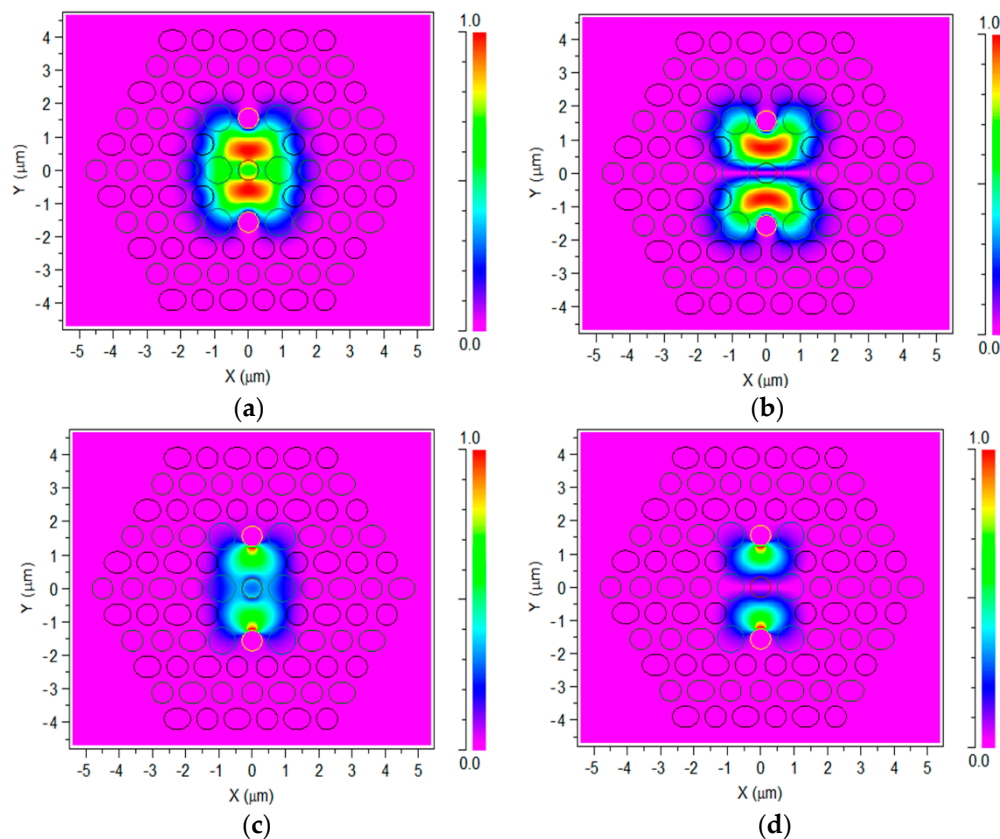


Figure 13. (a) Even-mode of x -direction, (b) odd-mode of x -direction, (c) even-mode of y -direction, and (d) odd-mode of y -direction for PS.

4. Conclusions

In conclusion, a novel ultra-short PS based on Ti and liquid infiltrated PCF with high birefringence have been demonstrated by using a vector beam propagation method. The designed PS shows an ultra-short length of 83.9 μm , a coupling loss of 0.0068 dB, a high extinction ratio of -44.05 dB, and a bandwidth of 32.1 nm at a wavelength of 1.55 μm . In addition, the birefringence of PS can attain the order 10^{-2} at the wavelength of 1.55 μm . The ultra-short PS with highly birefringent and low coupling

loss properties is suitable for optical sensing, communication systems, storage systems, and integrated circuit systems.

Author Contributions: Analysis and writing, Q.X.; data curation, W.L.; project administration, S.L.; methodology, K.L. and N.C.

Funding: This work is supported by the National Natural Science Foundation of China (Grant No. 11647008) and the Scientific Research Program funded by Shaanxi Provincial Education Department (Grant No. 18JK0042).

Conflicts of Interest: The authors declare no conflicts of interest.

References

- Hu, D.J.J.; Pui, H. Recent advances in plasmonic photonic crystal fiber: Design, fabrication and applications. *Adv. Opt. Photonics* **2017**, *9*, 259–314. [[CrossRef](#)]
- Knight, J.C. Photonic crystal fiber. *Nature* **2003**, *424*, 847–851. [[CrossRef](#)]
- Russell, P. Photonic crystal fiber. *Science* **2003**, *299*, 358–362. [[CrossRef](#)] [[PubMed](#)]
- Kurokawa, K. Optical Fiber for High-Power Optical Communication. *Crystals* **2012**, *2*, 1382–1392. [[CrossRef](#)]
- Chiang, J. Analysis of Leaky Modes in Photonic Crystal Fibers Using the Surface Integral Equation Method. *Crystals* **2018**, *8*, 177. [[CrossRef](#)]
- Yu, Y.; Sun, B. Ultra-Wide-Bandwidth Tunable Magnetic Fluid-Filled Hybrid Connected Dual-Core Photonic Crystal Fiber Mode Converter. *Crystals* **2018**, *8*, 95.
- Zhang, H.; Zhang, X.; Li, H.; Deng, Y.; Xi, L.; Tang, X.; Zhang, W. The Orbital Angular Momentum Modes Supporting Fibers Based on the Photonic Crystal Fiber Structure. *Crystals* **2017**, *7*, 286. [[CrossRef](#)]
- Islam, M.S.; Sultana, J.; Dinovitser, A.; Faisal, M.; Islam, M.R.; Ng, B.W.; Abbott, D. Zeonex-based asymmetrical terahertz photonic crystal fiber for multichannel communication and polarization maintaining applications. *Appl. Opt.* **2018**, *4*, 666–672. [[CrossRef](#)]
- Liu, Q.; Li, S.; Shi, M. Fiber Sagnac interferometer based on a liquid-filled photonic crystal fiber for temperature sensing. *Opt. Commun.* **2016**, *381*, 1–6. [[CrossRef](#)]
- Sun, B.; Chen, M.; Zhang, Y.; Zhou, J. Polarization-dependent coupling characteristics of metal-wire filled dual-core photonic crystal fiber. *Opt. Quantum Electron.* **2015**, *47*, 441–451. [[CrossRef](#)]
- Fan, Z.; Li, S.; Liu, Q.; Chen, H.; Wang, X. Plasmonic broadband polarization splitter based on dual-core photonic crystal fiber with elliptical metallic nanowires. *Plasmonics* **2016**, *11*, 1565–1572. [[CrossRef](#)]
- Huang, Y.; Xu, Y.; Yariv, A. Fabrication of functional microstructured optical fibers through a selective-filling technique. *Appl. Phys. Lett.* **2004**, *85*, 5182–5184. [[CrossRef](#)]
- Sultana, J.; Islam, M.S.; Ahmed, K.; Dinovitser, A. Terahertz detection of alcohol using a photonic crystal fiber sensor. *Appl. Opt.* **2018**, *57*, 2426–2431. [[CrossRef](#)]
- Haakestad, M.W.; Alkeskjold, T.T.; Nielsen, M.D.; Scolari, L.; Riishede, J.; Engan, H.E.; Bjarklev, A. Electrically tunable photonic bandgap guidance in a liquid-crystal-filled photonic crystal fiber. *IEEE Photonics Technol. Lett.* **2005**, *17*, 819–821. [[CrossRef](#)]
- Fan, Z.; Li, S.; Zhang, W.; An, G.; Bao, Y. Analysis of the polarization beam splitter in two communication bands based on ultrahigh birefringence dual-core tellurite glass photonic crystal fiber. *Opt. Commun.* **2014**, *333*, 26–31. [[CrossRef](#)]
- Chen, M.; Yu, R.; Zhao, A. Highly birefringence rectangular lattice photonic crystal fiber. *J. Opt. A Pure Appl. Opt.* **2004**, *6*, 997–1000. [[CrossRef](#)]
- Kim, S.; Kee, C.; Lee, C.G. Modified rectangular lattice photonic crystal fibers with high birefringence and negative dispersion. *Opt. Express* **2009**, *17*, 7952–7957. [[CrossRef](#)]
- Yang, T.; Wang, E.; Jiang, H.; Hu, Z.; Xie, K. High birefringence photonic crystal fiber with high nonlinearity and low confinement loss. *Opt. Express* **2009**, *23*, 8329–8337. [[CrossRef](#)] [[PubMed](#)]
- Jiang, L.; Zheng, Y.; Yang, J.; Hou, L.; Li, Z.; Zhao, X. An ultra-broadband single polarization filter based on plasmonic photonic crystal fiber with a liquid crystal core. *Plasmonics* **2017**, *12*, 411–417. [[CrossRef](#)]
- Chiang, J.; Sun, N.; Lin, S.; Liu, W. Analysis of an ultrashort PCF-based polarization splitter. *J. Lightw. Technol.* **2010**, *28*, 707–713. [[CrossRef](#)]
- Wu, H.; Tan, Y.; Dai, D. Ultra-broadband high-performance polarizing beam splitter on silicon. *Opt. Express* **2017**, *25*, 6069–6075. [[CrossRef](#)] [[PubMed](#)]

22. Jun, D.; Zhang, Z.; Zheng, H.; Sun, M. Recent progress on plasmon-enhanced fluorescence. *Nanophotonics* **2015**, *4*, 472–490.
23. Zhang, Y.; He, Y.; Wu, J.; Jiang, X.; Liu, R.; Qiu, C.; Jiang, X.; Yang, J.; Tremblay, C.; Su, Y. High-extinction-ratio silicon polarization beam splitter with tolerance to waveguide width and coupling length variations. *Opt. Express* **2016**, *24*, 6586–6593. [[CrossRef](#)] [[PubMed](#)]
24. Tanizawa, K.; Suzuki, K.; Ikeda, K.; Namiki, S.; Kawashima, H. Non-duplicate polarization-diversity 8×8 Si-wire PILOSS switch integrated with polarization splitter-rotators. *Opt. Express* **2017**, *25*, 10885–10892. [[CrossRef](#)]
25. González-Vila, Á.; Kinet, D.; Mégret, P.; Caucheteur, C. Narrowband interrogation of plasmonic optical fiber biosensors based on spectral combs. *Opt. Laser Technol.* **2017**, *96*, 141–146. [[CrossRef](#)]
26. Lu, X.; Soto, M.A.; Thévenaz, L. Temperature-strain discrimination in distributed optical fiber sensing using phase-sensitive optical time-domain reflectometry. *Opt. Express* **2017**, *25*, 16059–16071. [[CrossRef](#)]
27. Huang, Z.; Yang, X.; Wang, Y.; Meng, X.; Fan, R.; Wang, L. Ultrahigh extinction ratio of polarization beam splitter based on hybrid photonic crystal waveguide structures. *Opt. Commun.* **2015**, *354*, 9–13. [[CrossRef](#)]
28. Zhang, L.; Yang, C. Polarization splitter based on photonic crystal fibers. *Opt. Express* **2003**, *9*, 1015–1020. [[CrossRef](#)]
29. Li, J.; Wang, J.; Wang, R.; Liu, Y. A novel polarization splitter based on dual-core hybrid photonic crystal fibers. *Opt. Laser Technol.* **2011**, *43*, 795–800. [[CrossRef](#)]
30. Liu, S.; Li, S.; Yin, G.; Feng, R.; Wang, X. A novel polarization splitter in ZnTe tellurite glass three-core photonic crystal fiber. *Opt. Commun.* **2012**, *285*, 1097–1102. [[CrossRef](#)]
31. Zi, J.; Li, S.; An, G.; Fan, Z. Short-length polarization splitter based on dual-core photonic crystal fiber with hexagonal lattice. *Opt. Commun.* **2016**, *363*, 80–84. [[CrossRef](#)]
32. Xu, Z.; Li, X.; Ling, W.; Zhang, Z. Design of short polarization splitter based on dual-core photonic crystal fiber with ultra-high extinction ratio. *Opt. Commun.* **2015**, *354*, 314–320. [[CrossRef](#)]
33. Jiang, H.; Wang, E.; Zhang, J.; Hu, L.; Mao, Q.; Li, Q.; Xie, K. Polarization splitter based on dual-core photonic crystal fiber. *Opt. Express* **2014**, *22*, 30461–30466. [[CrossRef](#)] [[PubMed](#)]
34. Jiang, L.; Zheng, Y.; Hou, L.; Zheng, K.; Peng, J.; Zhao, X. An ultrabroadband polarization splitter based on square-lattice dual-core photonic crystal fiber with a gold wire. *Opt. Commun.* **2015**, *351*, 50–56. [[CrossRef](#)]
35. Sheng, Z.; Wang, J.; Feng, R. Design of a compact polarization splitter based on the dual-elliptical-core photonic crystal fiber. *Infrared Phys. Technol.* **2014**, *67*, 560–565. [[CrossRef](#)]
36. Vorobyev, A.Y.; Guo, C. Shot-to-shot correlation of residual energy and optical absorptance in femtosecond laser ablation. *Appl. Phys.* **2007**, *86*, 235–241. [[CrossRef](#)]
37. Zinger, O.; Zhao, G.; Schwartz, Z.; Simpson, J.; Wieland, M.; Landolt, D.; Boyan, B. Differential regulation of osteoblasts by substrate microstructural features. *Biomaterials* **2005**, *26*, 1837–1847. [[CrossRef](#)]
38. Ali, N.; Bashir, S.; Begum, N.; Rafique, M.S.; Husinsky, W. Effect of liquid environment on the titanium surface modification by laser ablation. *Appl. Surf. Sci.* **2017**, *405*, 298–307. [[CrossRef](#)]
39. Feit, M.D.; Fleck, J.A., Jr. Light propagation in graded-index optical fiber. *Appl. Opt.* **1978**, *24*, 3990–3998. [[CrossRef](#)]
40. Xiao, J.; Sun, X. A Modified full-vectorial finite-difference beam propagation method based on H-fields for optical waveguides with step-index profiles. *Opt. Commun.* **2006**, *266*, 505–511. [[CrossRef](#)]
41. Xie, K.; Boardman, A.D.; Xie, M.; Yang, Y.J.; Jiang, H.M.; Yang, H.J.; Wen, G.J.; Li, J.; Chen, K.; Chen, F.S. A Simulation of longitudinally magnetized three-dimensional magneto-optical devices by a full-vectorial beam propagation method. *Opt. Commun.* **2008**, *281*, 3275–3285. [[CrossRef](#)]
42. Sani, E.; Dell’Oro, A. Spectral optical constants of ethanol and isopropanol from ultraviolet to far infrared. *Opt. Mater.* **2016**, *60*, 137–141. [[CrossRef](#)]
43. Rakić, A.D.; Djurišić, A.B.; Elazar, J.M.; Majewski, M.L. Optical properties of metallic films for vertical-cavity optoelectronic devices. *Appl. Opt.* **1998**, *37*, 5271–5283. [[CrossRef](#)] [[PubMed](#)]
44. Saitoh, K.; Sato, Y.; Koshiba, M. Coupling characteristics of dual-core photonic crystal fiber couplers. *Opt. Express* **2003**, *11*, 3188–3195. [[CrossRef](#)]
45. Eisenmann, M.; Weidel, E. Single-mode fused biconical coupler optimized for polarization beam splitting. *J. Lightw. Technol.* **1991**, *9*, 853–858. [[CrossRef](#)]
46. Saitoh, K.; Sato, Y.; Koshiba, M. Polarization splitter in three-core photonic crystal fibers. *Opt. Express* **2004**, *12*, 3940–3946. [[CrossRef](#)]

47. Zhang, Y.; Li, K.; Wang, L.; Ren, L.; Zhao, W.; Miao, R.; Large, M.C.J.; Eijkelenborg, M.A.V. Casting preforms for microstructured polymer optical fibre fabrication. *Opt. Express* **2006**, *14*, 5541–5547. [[CrossRef](#)]
48. Chen, X.; Li, M.; Koh, J.; Nolan, D.A. Wide band single polarization and polarization maintaining fibers using stress rods and air holes. *Opt. Express* **2008**, *16*, 12060–12068. [[CrossRef](#)]
49. Zhang, S.; Yu, X.; Zhang, Y.; Shum, P.; Zhang, Y. Theoretical study of dual-core photonic crystal fibers with metal wire. *IEEE Photonics J.* **2012**, *4*, 1178–1187. [[CrossRef](#)]



© 2019 by the authors. Licensee MDPI, Basel, Switzerland. This article is an open access article distributed under the terms and conditions of the Creative Commons Attribution (CC BY) license (<http://creativecommons.org/licenses/by/4.0/>).